Received: 6 May 2021 | Revised: 20 July 2021 | Accepted: 26 July 2021

DOI: 10.1002/mrm.28968

RESEARCH ARTICLE

Magnetic Resonance in Medicine

Rapid safety assessment and mitigation of radiofrequency induced implant heating using small root mean square sensors and the sensor matrix Q_S

Berk Silemek[1] | Frank Seifert[1] | Johannes Petzold[1] | Werner Hoffmann[1] | Harald Pfeiffer[1] | Oliver Speck[2,3,4,5] | Georg Rose[5,6] | Bernd Ittermann[1] | Lukas Winter[1]

[1]Physikalisch-Technische Bundesanstalt (PTB), Braunschweig and Berlin, Germany

[2]Biomedical Magnetic Resonance, Otto-von-Guericke-University Magdeburg, Magdeburg, Germany

[3]German Center for Neurodegenerative Diseases (DZNE), Magdeburg, Germany

[4]Leibniz Institute for Neurobiology (LIN), Magdeburg, Germany

[5]Center for Behavioral Brain Sciences (CBBS), Magdeburg, Germany

[6]Institute for Medical Engineering and Research Campus STIMULATE, University of Magdeburg, Magdeburg, Germany

Correspondence
Lukas Winter, Physikalisch-Technische Bundesanstalt (PTB), Abbestr. 2-12, 10587 Berlin, Germany.
Email: Lukas.winter@ptb.de

Funding information
European Association of National Metrology Institutes, Grant/Award Number: 17IND01 MIMAS

Purpose: Rapid detection and mitigation of radiofrequency (RF)-induced implant heating during MRI based on small and low-cost embedded sensors.

Theory and Methods: A diode and a thermistor are embedded at the tip of an elongated mock implant. RF-induced voltages or temperature change measured by these root mean square (RMS) sensors are used to construct the sensor Q-Matrix (Q_S). Hazard prediction, monitoring and parallel transmit (pTx)-based mitigation using these sensors is demonstrated in benchtop measurements at 300 MHz and within a 3T MRI.

Results: Q_S acquisition and mitigation can be performed in <20 ms demonstrating real-time capability. The acquisitions can be performed using safe low powers (<3 W) due to the high reading precision of the diode (126 μV) and thermistor (26 μK). The orthogonal projection method used for pTx mitigation was able to reduce the induced signals and temperatures in all 155 investigated locations. Using the Q_S approach in a pTx capable 3T MRI with either a two-channel body coil or an eight-channel head coil, RF-induced heating was successfully assessed, monitored and mitigated while the image quality outside the implant region was preserved.

Conclusion: Small (<1.5 mm^3) and low-cost (<1 €) RMS sensors embedded in an implant can provide all relevant information to predict, monitor and mitigate RF-induced heating in implants, while preserving image quality. The proposed pTx-based Q_S approach is independent of simulations or in vitro testing and therefore complements these existing safety assessments.

KEYWORDS
active implantable medical devices, implant safety, interventional MRI, MR safety, parallel transmission, RF heating

1 | INTRODUCTION

Radiofrequency (RF) -induced heating of implants or interventional devices during an MRI exam is a well-known safety risk affecting a large patient population.[1,2] The current approach to safely scan patients with implants relies on offline testing as described in ISO/TS 10974 or ASTM F2182.[3,4] These standards provide reliable procedures to ensure the safety of patients with implants in most scenarios. However, these tests are time-consuming and costly; they often result in exposure restrictions and, most importantly, leave it to the responsibility of the MR operator to ensure compliance with these limits. Furthermore, safety guidelines are based on reasonable assumptions and always need to account for uncertainties,[3,5] resulting in conservative RF limits degrading image quality or extending scan times more than may be necessary individually. Since the benefits of MRI frequently outweigh the risks even in patients with active implants, studies are pushing the limits toward MRI of patients with cardiac implantable electronic devices,[6-10] or deep brain stimulators (DBS).[11-20] Nevertheless, reliable techniques are still needed, mitigating RF-induced implant heating with minimum detrimental effect on diagnostic image quality.

Many such approaches are based on parallel transmission (pTx) systems, which were introduced two decades ago, increasing the degree of freedom to shape the RF excitation field in the target region of interest.[21-24] Adjusting the amplitudes and phases of RF pulses transmitted to individual channels of a pTx coil properly, the background *E*-field along and hence the RF-induced currents within an implant can be minimized. RF-induced heating is thus substantially reduced while simultaneously the overall image quality can be largely preserved.[1,25-32] To optimize the RF excitation for heating reduction, the induced current, field or temperature needs to be known.

Frequently, this information is deduced from electromagnetic simulations. In earlier studies, optimization algorithms were proposed to shim RF channels in homogeneous[33] and heterogenous[34,35] phantoms in the presence of simple wires. In a more complex simulation model, DBS lead trajectories were extracted from computed tomography images, demonstrating the principle feasibility of pTx-based mitigation in a more realistic setting.[36,37] Although these simulation studies provide encouraging results, in a real patient exam the induced currents may still be strongly affected by inaccuracies in the patient and implant model together with subject motion or implant position.[38-40]

Another approach is to measure relevant variables for pTx-based SAR-mitigation during an MRI exam in the patient. MR image artifacts around electrically conductive implants can be used to quantify its internal currents,[41,42] which then allows modification of the pulses to reduce RF-induced implant heating.[43-48] Another pTx-based mitigation approach is using sensors to measure the fields around[29] or currents inside[28,49] implants. With this sensor information, so-called "null mode" (NM) excitation can be performed, which reduces tip heating substantially.[28,49] A recent study proposed the so-called "orthogonal projection" (OP) method as a pTx mitigation tool based on time-domain *E*-field probe measurements outside the implant.[29] The OP method projects a homogeneous excitation vector, eg, the circular polarization mode (CP) or a B_1^+-shim, onto the subspace orthogonal to a worst-case excitation (producing maximum implant heating), thus preserving imaging quality while reducing tip heating.[29]

So far, these existing methods were demonstrated by using bulky time-domain sensors that could not be placed directly at the hot-spot location (ie, the implant tip). Root mean square (RMS) sensors, on the other hand, offer more flexible design options as they have smaller footprint and simpler acquisition electronics. For example, six temperature measurement probes have been embedded into the tip of an RF ablation electrode of 2.5 mm diameter.[50,51]

In this work, we demonstrate how small (<1.5 mm^3) and low-cost (<1 €) RMS sensors such as a diode[52,53] and a thermistor,[53,54] embedded in a mock implant, can be used for safety assessments. We introduce the sensor Q matrix ($\boldsymbol{Q_S}$), constructed from measured sensor data, which fully characterizes the implant related hazard and allows to predict and mitigate RF-induced heating. We show in testbed measurements at $f = 300$ MHz and in 3T scanner experiments that $\boldsymbol{Q_S}$ can be rapidly utilized to perform NM-based or OP-based mitigation strategies. Our results suggest that such embedded sensors together with $\boldsymbol{Q_S}$ can be used as a novel implant safety strategy in which the implant communicates with the MR scanner to assess and reduce the risks associated with RF-induced implant heating. In principle, this approach does not need any additional information based on electromagnetic field simulations or in vitro safety testing procedures.

2 | THEORY

For an *N*-channel pTx excitation in MRI, the local SAR depends on the superposition of the complex valued *E*-fields

generated by each channel and can be expressed using the Q-Matrix formulation.[55]

$$\mathrm{SAR} = \boldsymbol{u}^{\boldsymbol{H}}\boldsymbol{Q}\boldsymbol{u}, \tag{1}$$

where $\vec{u}$ is the complex valued excitation vector, H denotes Hermitian transposition, and $\boldsymbol{Q}$ is the Q-Matrix,[22,55,56] which is a positive definitive Hermitian matrix. Once $\boldsymbol{Q}$ is computed for a position of interest, local SAR can be calculated for any excitation vector $\boldsymbol{u}$. This formulation is well suited for patient specific safety calculations because it eliminates the need to repeat the time-consuming simulations for each possible pTx excitation vector.[55] Here, we demonstrate how the Q-matrix concept can be translated to implants with embedded RMS sensors allowing measurement-based pTx mitigation of RF-induced heating.

For an elongated implant like an electrode or lead, the SAR hotspot is usually found at the distal tip of the implant.[1,57] If a safety-relevant physical quantity, eg, E-field or temperature, can be measured at this location by a suitable sensor, the response of the implant to an pTx excitation can be deduced. A matrix can then be constructed from these measurands in full analogy to the Q-matrix from Equation (1):

$$X = \boldsymbol{u}^{\boldsymbol{H}}\boldsymbol{Q}_{\boldsymbol{S}}\boldsymbol{u}, \tag{2}$$

where X denotes the sensor reading. Since RMS sensors provide no phase information, N^2 measurements are required to construct the Hermitian $\boldsymbol{Q}_{\boldsymbol{S}}$ for an N-channel pTx system:

$$Q^{X}_{S,kl} = \begin{cases} \left(X_{kl} - X_k - X_l\right) + j\left(X^{\dagger}_{kl} - X_k - X_l\right) & \text{for } k \neq l \text{ and } k < l \\ \left(X_{kl} - X_k - X_l\right) - j\left(X^{\dagger}_{kl} - X_k - X_l\right) & \text{for } k \neq l \text{ and } k > l \\ 2X_k & \text{for } k = l \end{cases}, \tag{3}$$

where X_k is the sensor reading when only channel k transmits, X_{kl} denotes the sensor reading when channels k and l transmit simultaneously in phase, and $X^{\dagger}_{kl}$ the same for a $\pi/2$ phase difference between both channels, while the channels' amplitudes are always identical. The measurands in the matrix can be either rectified voltages using a diode or temperatures using a thermistor. Voltages probe the local E-field and their square value is thus proportional to SAR; measuring $T(t)$ for a short period of time gives the temperature change rate dT/dt, also proportional to SAR.[58,59] As a result, $\boldsymbol{Q}_{\boldsymbol{S}}$ exists in two flavors, $\boldsymbol{Q}^{\boldsymbol{E}}_{\boldsymbol{S}}$ and $\boldsymbol{Q}^{\boldsymbol{T}}_{\boldsymbol{S}}$. which can be used to predict the E-field or dT/dt, respectively, at the most critical position, the implant tip, for any pTx excitation via Equation (2). For pTx-based mitigation, eigenvalue decomposition of $\boldsymbol{Q}_{\boldsymbol{S}}$ is obtained by calculating the eigenvalues (λ) and eigenvectors ($\boldsymbol{v}$):

$$\boldsymbol{Q}_{\boldsymbol{S}}\boldsymbol{v} = \lambda\boldsymbol{v}. \tag{4}$$

With this information, two methods (OP[26,29] and NM[28]) have been applied. The OP method is based on an orthogonal projection of a vector used for imaging (eg, CP) to a worst-case (WC) voltage vector $\boldsymbol{u}_{\boldsymbol{WC}}$, ie, the eigenvector with the largest eigenvalue of $\boldsymbol{Q}_{\boldsymbol{S}}$:

$$\boldsymbol{u}_{\boldsymbol{OP}} = \boldsymbol{u}_{\boldsymbol{CP}} - \boldsymbol{u}_{\boldsymbol{WC}}\left(\boldsymbol{u}_{\boldsymbol{WC}} \cdot \boldsymbol{u}_{\boldsymbol{CP}}\right). \tag{5}$$

For the null modes with one observation/null location (ie, one sensor at the implant tip) $N - 1$ null modes exist.[28] For simplicity, one NM is extracted using singular value decomposition of $\boldsymbol{Q}_{\boldsymbol{S}}$ and then, the null space vector of the lowest eigenvalue has been used as an excitation vector. While NM is a pure safety strategy, the OP method aims to combine safety with B_1^+ fidelity, preserved from the projected imaging vector.

3 | METHODS

The feasibility of the $\boldsymbol{Q}_{\boldsymbol{S}}$ approach is demonstrated experimentally using an implant safety testbed[29] (Figure 1) and a 3T scanner (Figure 2).

3.1 | Implants and sensors

Two mock implants (Figure 3) were used to mimic a longitudinal implant with an RF-induced hotspot at its tip:

1. A CAT-8 (Figure 3A) cable with 2.5 mm of insulation removed at its tip. This cable has four shielded twisted-pair wires, two of them were used to embed a Schottky diode (MMDL101T1G, ON Semiconductor, Phoenix, AZ, US) and a thermistor (negative termperature coefficient [NTC], 10 kΩ: 25℃, NCP18XH103F03RB, Murata, Nagaokakyo, Japan) (Figure 3B). The Schottky diode was soldered with the cathode to the wire and a 2.5 mm copper wire was soldered to the anode to increase its sensitivity for the lower peak amplitude testbed measurements (Figure 3B). The E-fields at the implant tip lead to an induced voltage that can be rectified by the Schottky diode and measured at the end of the cable.[60-62] The shield of the cable is used as a ground reference for the diode signal.
2. A semi-rigid coaxial cable (Figure 3C) with an embedded thermistor (NTC, 10 kΩ: 25℃, NCP18XH103F03RB, Murata, Nagaokakyo, Japan) connected between inner and outer conductor at the implant tip (Figure 3D). Around the tip 15 mm of insulation was removed.

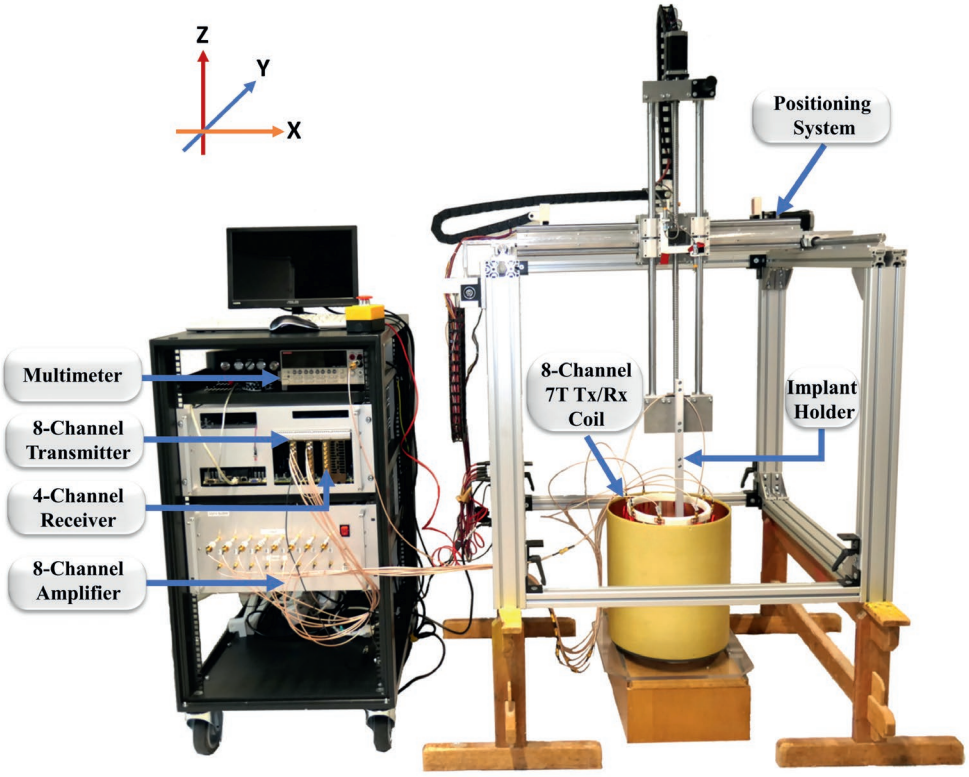

FIGURE 1 Experimental setup for the pTx testbed experiments at 300 MHz (B_0 = 7.0T). The testbed has an eight-channel arbitrary waveform generator, eight 20 W broadband RF power amplifiers and a four-channel receiver.[29] For transmission an eight-channel pTx RF coil was used, loaded with a cylindrical PVP phantom.[29,60] A digital multimeter was used to measure the resistance of the thermistor and the receiver card (synchronized with the transmitters) was used to measure the diode signal. All pTx pulses were generated by the console, which was also controlling the positioning system COSI Measure[61] using a TCP/IP communication protocol. This allowed for automated 2D/3D mapping experiments of multiple implant locations

3.2 | Testbed experiments

3.2.1 | Instrumentation

An eight-channel pTx implant safety testbed (Figure 1) was used for experiments at 300 MHz.[29] The RF coil[63] was loaded with a cylindrical (diameter 200 mm, height 198 mm) polyvinylpyrrolidone (PVP) phantom ($\varepsilon = 43.80$, $\sigma = 0.35$ S/m) and the mock implant 1 was immersed in the phantom using the positioning system COSI Measure.[64]

3.2.2 | Diode measurements ($\boldsymbol{Q}_S^E$)

The precision for the diode measurements is 126 µV with a dynamic range of 1 V and a temporal resolution of 4 µs. For transmission, an RF pulse train (2.86 W per channel) with 200 µs rectangular pulses and a repetition time (TR) of 300 µs was used. For an eight-channel pTx coil, $N^2 = 64$ pulses were transmitted to construct a single $\boldsymbol{Q}_S^E$. The 14-bit ADC from the receiver cards of the testbed (4 MHz sampling frequency) was used to acquire the signal and the total acquisition time for $\boldsymbol{Q}_S^E$ was 19.2 ms.

3.2.3 | Temperature measurements ($\boldsymbol{Q}_S^T$)

For temperature measurements, the resistance over a thermistor was measured using a digital multimeter (Keithley 2000, Tektronix, Beaverton, OR, US). The thermistor had previously been benchmarked against fiber optic temperature probes using implant 2.[29] In this study, the twisted-pair cables connecting the thermistor to the multimeter are shielded to reduce RF interference in temperature measurements. The temperature measurements have 26 µK resolution with a precision of 100 µK and a temporal resolution of 40 ms. Rectangular RF pulses (duration 0.5 s, 2.86 W per channel) were followed by a 0.5 s cooling period. Total acquisition time for a $\boldsymbol{Q}_S^T$ is 64 s. Since $\boldsymbol{Q}_S^T$ intends to capture the response function of the implant, background temperature variations may affect the measurements for longer experiments or multiple implant locations. Therefore, the baseline temperature drift was determined and subtracted from the temperature gradient for each pulse. To investigate repeatability, $\boldsymbol{Q}_S^T$ was measured ten times at the same implant location with a 120 s break between consecutive acquisitions.

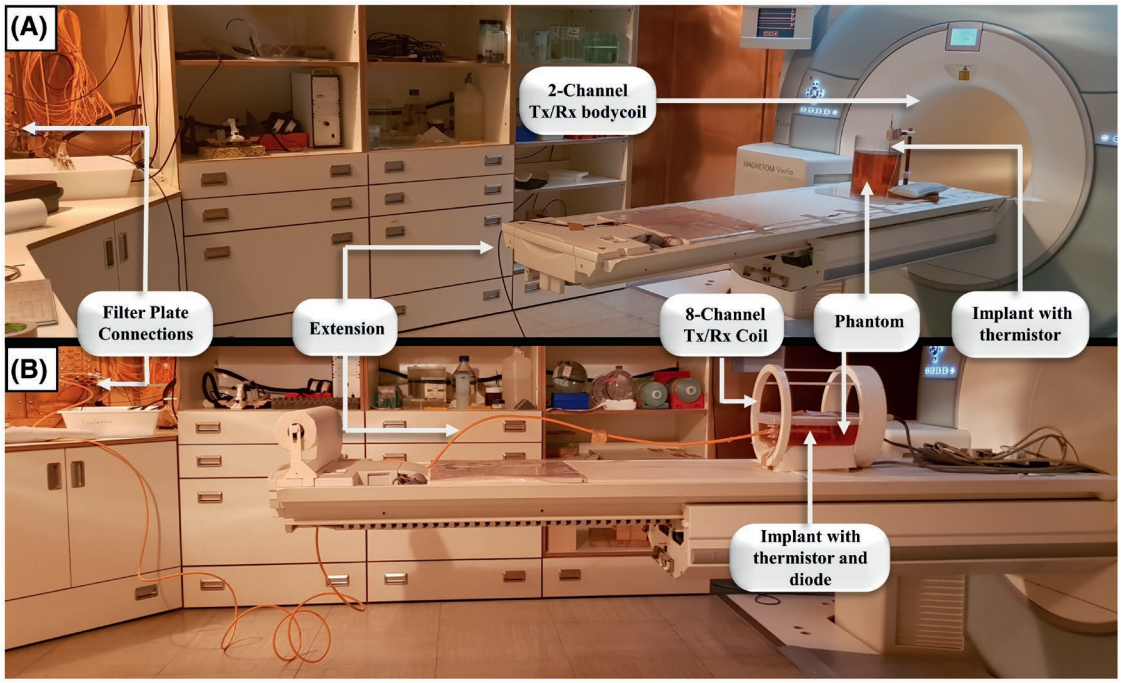

FIGURE 2 Experimental setup within a pTx capable 3T MRI. Two different configurations were investigated: Transmission with a pTx capable two-channel body coil, a cylindrical phantom and guidewire substitute as mock implant with embedded thermistor (A) and transmission using an eight-channel Tx/Rx RF coil, a rectangular phantom and a mock implant with embedded diode and thermistor (B)

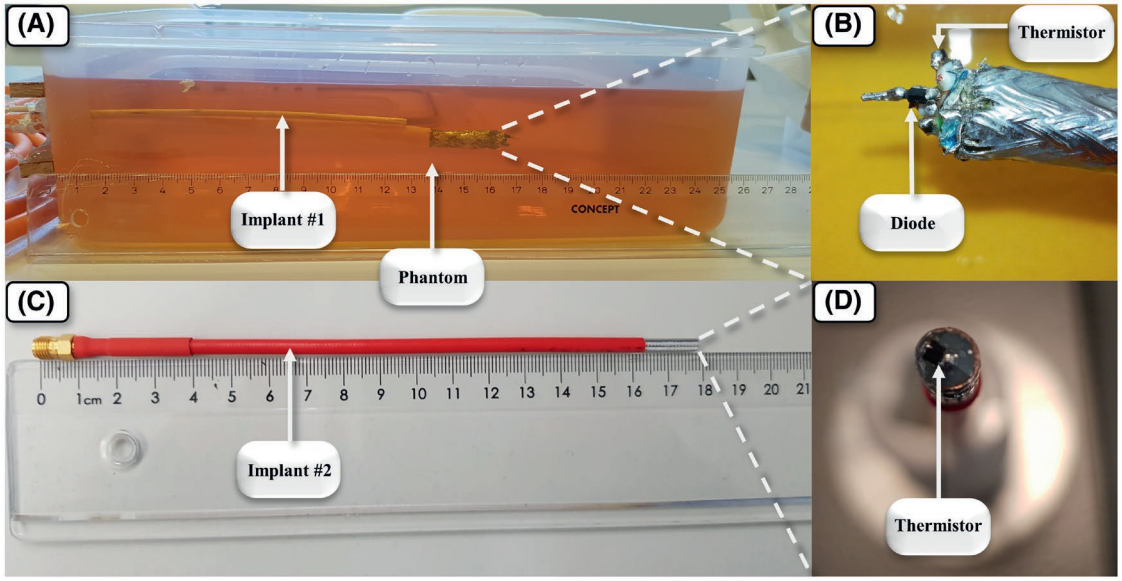

FIGURE 3 Photos of the mock implants with embedded RMS sensors at the implant tip (diode and thermistor) for Q_S assessment, pTx mitigation and prediction of RF-induced heating. Photograph of a CAT-8 cable inside a PVP filled phantom (A) with embedded diode (1.70 mm × 1.25 mm) and thermistors (1.6 mm × 0.8 mm) at its tip (B). For the diode a small extension wire was added to increase its sensitivity in regions of low background E-fields for the lower peak power testbed measurements. This extension wire is not needed in an MRI, which has much higher transmitted amplitudes (see also Supporting Information Figure S3). For both thermistor and diode measurements a low pass filter was used. Photograph of a 180 mm long coaxial cable (C) with embedded thermistor at the tip (D)

3.2.4 | Sensor based pTx mitigation

For each implant position, Q_S^E and Q_S^T were used independently to calculate WC, OP,[29] and NM.[28] All three modes plus CP as a reference were successively transmitted, each with an average forward power $P = 2.86$ W. Subsequently, tip E-fields and temperatures were measured for all modes (WC, CP, OP, and NM) at the same implant position. This

pTx mitigation scheme was tested at several implant positions in the phantom. For $\boldsymbol{Q}_S^E$ mapping and mitigation, a 140 mm × 110 mm axial plane (see Figure 1) 120 mm below the liquid surface was mapped with 10 mm resolution. For the lengthier $\boldsymbol{Q}_S^T$ measurements, seven locations in that plane were investigated.

For each transmission mode (WC, CP, OP, NM) and implant location, an additional 2 s rectangular RF heating pulse with 2.86 W of forward power was applied to measure the tip temperature increase.

3.3 | MR experiments

To further investigate the feasibility of the approach, a series of MR experiments were performed on a pTx capable (eight-channel with 8 kW peak-power per channel) 3T scanner (Verio, Siemens Healthineers, Erlangen, Germany).

3.3.1 | $\boldsymbol{Q}_S^T$ acquisition and temperature prediction with a two-channel body coil

The MRI setup for the temperature experiments is shown in Figure 2A. Mock implant 2 was immersed 95 mm deep into the same cylindrical phantom container and connected to a digital multimeter via the filter plate and a low-pass filter (SLP-1.9+, Mini-Circuits, New York, USA).

First, the scanner was used in its normal operation applying the CP mode to investigate the correlation between thermistor-based temperature measurements and transmitted power under pulsed RF and gradient conditions. Gradient echo (GRE) sequences (TR = 15 ms, RF pulse length 2 ms) were run with nominal flip angles varying from 10° to 90° in 10° increments while RF-pulse shape and transmit power differences were measured with a pick-up coil and a fast ADC card (M3i.4142, Spectrum Instruments, Grosshansdorf, Germany). The temperature from the sensor was recorded, and the transmitted power calculated by integrating the sinc-shaped RF pulses from the pickup coil.

Second, the prediction of RF-induced heating based on $\boldsymbol{Q}_S^T$ was investigated by driving the birdcage body coil as a two-channel pTx coil using two channels of the eight-channel pTx system. For this two-channel system, $N^2 = 4$ measurements (RF pulse duration = 4 to 5 s, cooling time ∼ 2s, total acquisition time ∼ 30s) were needed to acquire $\boldsymbol{Q}_S^T$. Amplitude and phase of the RF channels were then modified, the corresponding RF heating determined and compared to the prediction based on $\boldsymbol{Q}_S^T$. This procedure was repeated at a second implant location.

3.3.2 | $\boldsymbol{Q}_S^E$ based mitigation and imaging with an eight-channel head coil

The experimental setup is shown in Figure 2B. An eight-channel pTx head coil (RAPID Biomedical, Rimpar, Germany) was used for transmission. Mock implant 1 was placed off-center in a plastic container (275 × 220 × 70) mm³ filled (filling height 65 mm) with the same PVP mixture. The implant is immersed 177 mm (30 mm under the phantom surface) inside the phantom and connected to the filter plate. Nine plastic tubes were integrated into the phantom (five PVP filled, four air filled) to generate some contrast.

$\boldsymbol{Q}_S^E$ was obtained by transmitting $N^2 = 64$ rectangular RF pulses ($V_{\text{peak}} = 15\text{V},\ \text{duration} = 200\,\mu\text{s}$) using an FID sequence.

This setup is used to test the feasibility of $\boldsymbol{Q}_S^E$ based pTx mitigation under MR conditions and to compare the image quality of different pTx modes (WC, B_1-shim, OP, and NM). It resembles the situation, where diagnostic information in an ROI near but not directly at the implant is desired. For this purpose, a B_1^+ mapping sequence (2D GRE, echo time [TE]/TR = 3/30 ms, FOV = 256 × 256 mm^2, in-plane resolution = (1 × 1) mm², slice thickness = 10 mm) was applied to calculate relative B_1^+ maps for each pTx channel. The B_1^+ shim was then defined as constructive interference of all single element B_1^+ fields at the central plastic tube. This B_1-shim setting was used as the reference imaging mode and to calculate the OP mode. For each transmission mode, a coronal and an axial 2D GRE image ($\text{TE/TR} = 4/11\,\text{ms},\ \text{FOV} = 300 \times 300\,\text{mm}^2$, in-plane resolution (0.6×0.6) mm^2, slice thickness 10 mm, 2 averages) was acquired, ie, a total of eight images. In each case, the total forward power measured by the scanner was set to $P_{\text{meas}} = 24 \pm 0.5\text{W}$ and the E-field at the implant tip was measured with the diode.

4 | RESULTS

4.1 | Testbed experiments

4.1.1 | $\boldsymbol{Q}_S^E$ acquisition

A raw acquisition to determine $\boldsymbol{Q}_S^E$ is shown in Figure 4A. In this particular case, only 44 of 64 two-channel combinations induced a detectable current in the wire. The resulting $\boldsymbol{Q}_S^E$ for this implant location is shown in Figure 4B. Channels 2 and 8 made the strongest contribution, while the induced signal from channels 4 to 6 was negligible. This result is reasonable since the implant was in the bottom half of the head coil near channels 1 to 3 and 8.

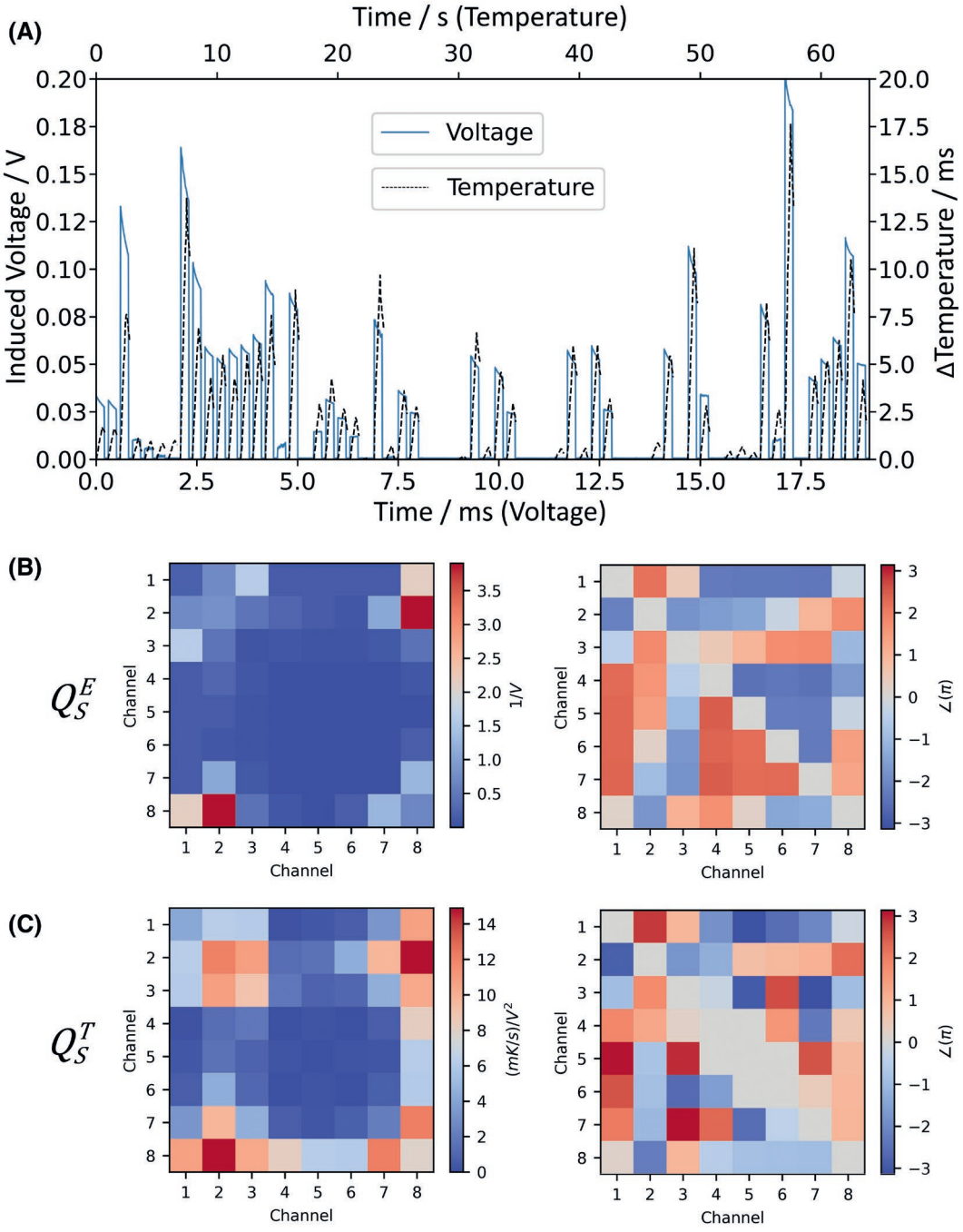

FIGURE 4 Q_S acquisition and evaluation based on the diode and thermistor signals in benchtop experiments at 300 MHz. A, Q_S acquisition (diode measurements are displayed with a solid blue line and 0.5 s thermistor readings with the same amplitude and phase are displayed with a dotted black line) for an eight-channel RF coil (64 RF pulses). The temperature and diode signals were independently acquired, and no calibration has been done and needed between temperature increase and diode voltage for pTx mitigation. Axes scales were adjusted only for visualization. Amplitudes and phases of the calculated $\boldsymbol{Q}_S^E$ (B) and $\boldsymbol{Q}_S^T$ (C). In both configurations a combination of channel 2 and channel 8 show the highest coupling to the implant. With respect to magnitude, the sensitivity of $\boldsymbol{Q}_S^T$ is higher compared to $\boldsymbol{Q}_S^E$, while the phases of dominant channels show similar values for both approaches

4.1.2 | $\boldsymbol{Q}_S^T$ acquisition

Amplitudes and phases from $\boldsymbol{Q}_S^T$ acquired at the same location are shown in Figure 4C. Here, 55 out 64 two-channel combinations create detectable temperature changes.

For ten consecutive $\boldsymbol{Q}_S^T$ acquisitions, the temperature curves are plotted atop of each other in Figure 5A, demonstrating the repeatability of the measurement. The maximum temperature increase during a single acquisition of ~ 1 min was $\Delta T = 82 \pm 0.8$ mK, indicating that

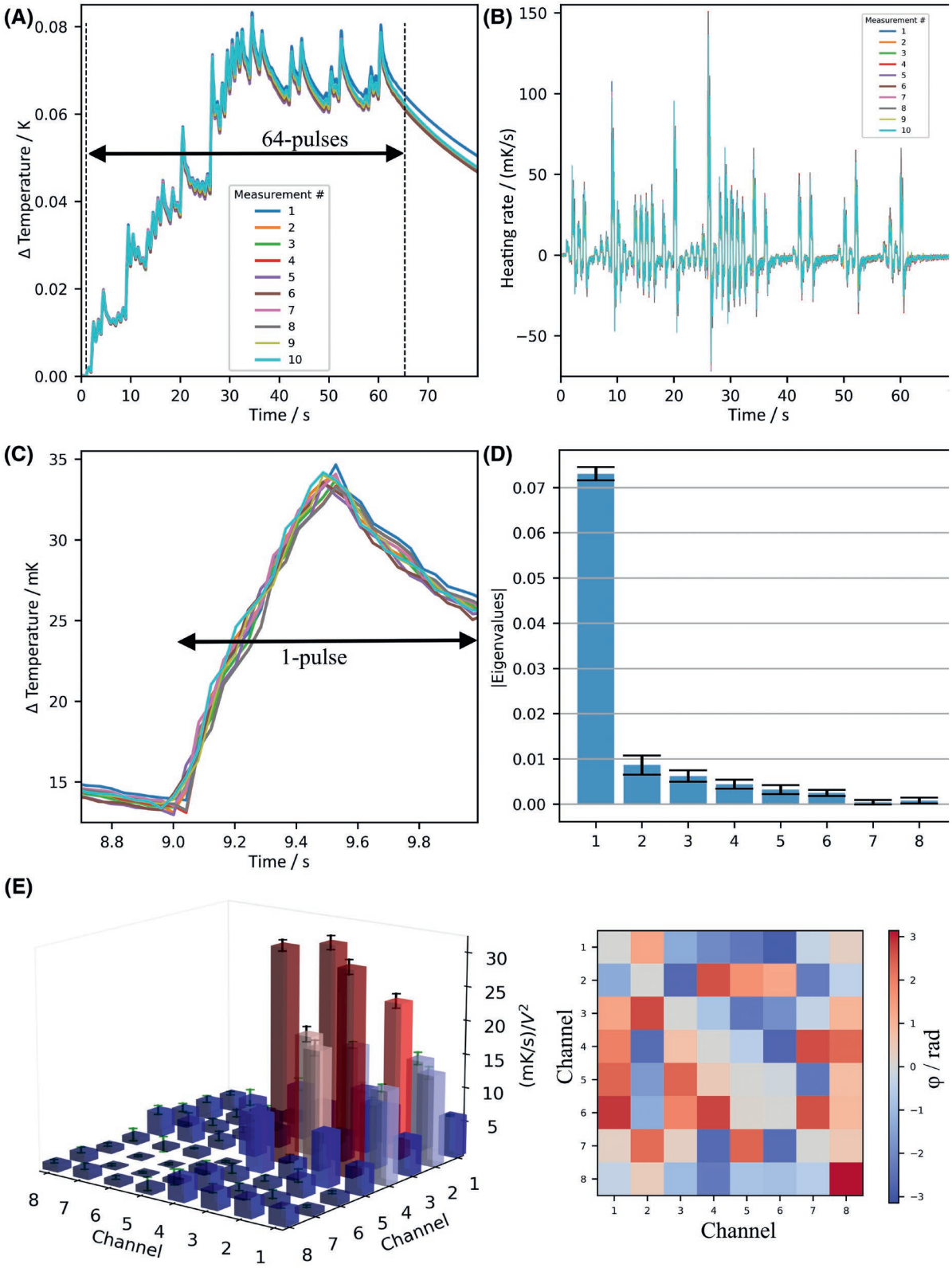

FIGURE 5 $\boldsymbol{Q}_S^T$ acquisition and repeatability based on thermistor readings in testbed experiments at 300 MHz. A, The dashed line shows the interval of the RF pulse train. Temperature readings for 64 consecutive RF pulses of 0.5 s followed by 0.5 s of cooling after each pulse. This sequence was repeated 10 times at the same location to analyze the reproducibility of the method. B, Heating rate dT/dt of a single $\boldsymbol{Q}_S^T$ acquisition (10 times repetition). C, Single cycle thermistor readings showing the sensitivity (26 μK) and precision (100 μK) of the thermistor readings. D, Calculated eigenvalues (normalized) including SD for the 10 repetitions of the $\boldsymbol{Q}_S^T$ acquisition. E, Amplitudes of the $\boldsymbol{Q}_S^T$ with error bars indicating the SD for all repetitions and phase of one $\boldsymbol{Q}_S^T$

$\boldsymbol{Q}_S^T$ can be acquired with negligible implant heating in a pre-scan. The extracted derivatives dT/dt from Figure 5A are depicted in Figure 5B. The sensor resolution is fully sufficient to capture such small heating effects without RF interference (cf. Ref. [29]), as is shown in Figure 5C where a mean slope of 13.9 ± 0.8 mK/s (5.5% SD over 10 repetitions) was determined for a single RF pulse. $\boldsymbol{Q}_S^T$ is calculated from these slopes and its eigenvalues and eigenvectors (Figure 5D) are then used to calculate the mitigation modes. The maximum normalized eigenvalue has a 73% weight in this particular case with a 2% SD over 10 measurements. The $\boldsymbol{Q}_S^T$ amplitudes are depicted in Figure 5E. The relative SDs increase for channel combinations with lower (and less significant) absolute heating rates.

4.1.3 | $\boldsymbol{Q}_S^E$ based pTx mitigation

The concept of $\boldsymbol{Q}_S^E$ based hazard mitigation is illustrated in Figure 6 where the sensor readings in an axial plane (x-y plane, Figure 1) of the cylindrical phantom are shown for different excitation modes. In CP mode (Figure 6A), the *E*-field signal is higher in implant locations near the phantom wall while a local minimum occurs in the central region.

Compared to this reference, the OP and NM modes with the same RF power reduce the sensor signal in all or 99% of the investigated locations, respectively. In two positions, NM produced a 14% and 18% higher sensor reading than CP. At the implant location ($x = 0, y = 0$) with the highest RF-induced values in CP mode, readings were 12 and 32 times lower for OP and NM, respectively. The highest measured

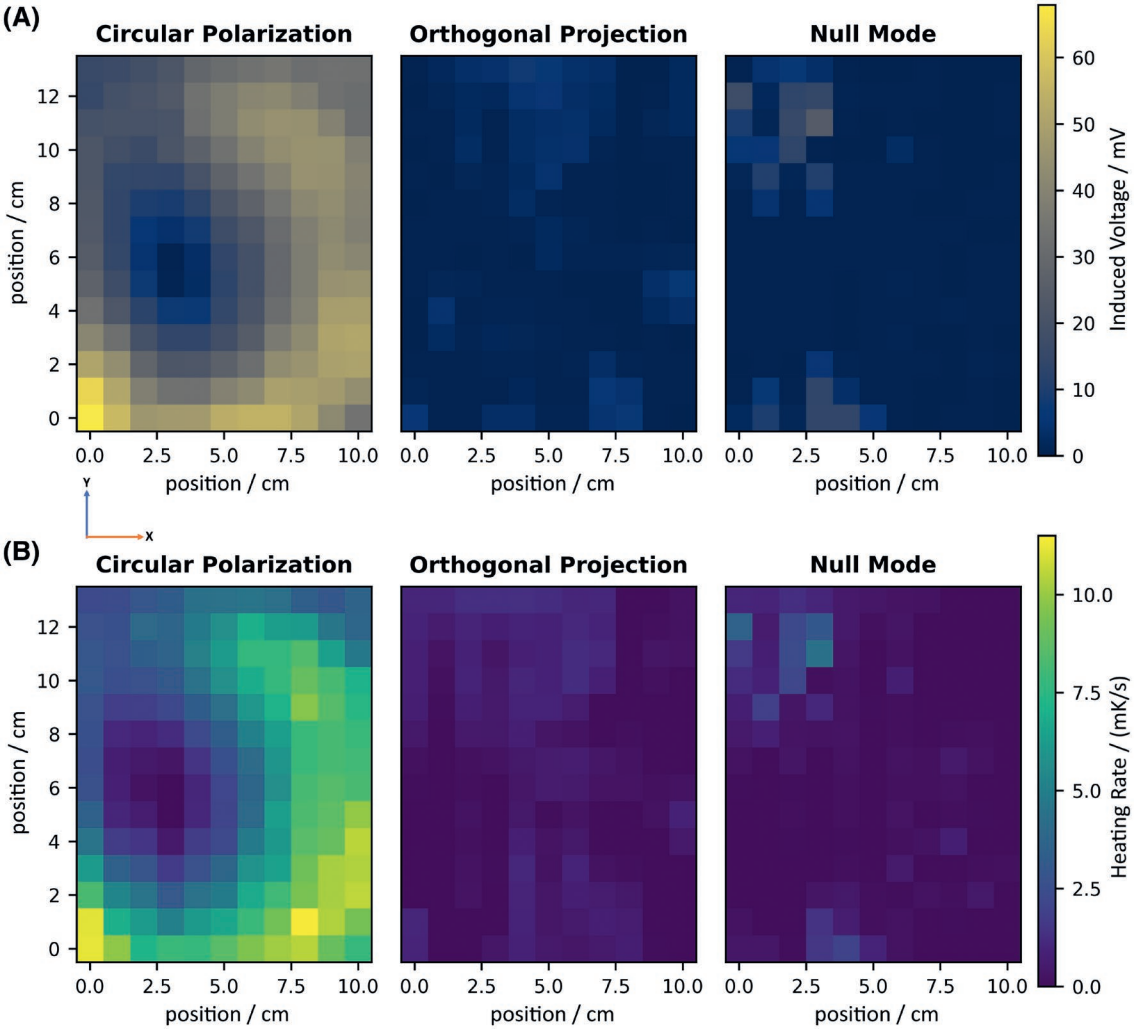

FIGURE 6 The results of the $\boldsymbol{Q}_S^E$ mapping experiment in a 110×140 mm^2 area with 10 mm resolution in the 300 MHz testbed. The implant is immersed 120 mm into the phantom. A, The induced voltage measurements from the modes CP, OP and NM are shown. The OP and NM are calculated and applied by using the acquired $\boldsymbol{Q}_S^E$. In B, The temperature change rate map of subsequent 2 s temperature experiments using the acquired $\boldsymbol{Q}_S^E$ for the CP, OP and NM are shown. The induced peak voltage measured over the diode correlates linearly (Pearson coefficient: r > 0.94, $P < .001$) with the square root of the heating rate measured with the thermistor

OP voltage was still four times lower than CP at that location ($x = 4, y = 13$).

For all three modes, the simultaneously measured heating rates (Figure 6B) correspond well to the diode signals (Figure 6A) indicating that the measured E-fields have insignificant RF interference to the pTx mitigations. The measured temperature time courses are depicted in Supporting Information Figure S1A, which is available online (absolute temperatures), and Supporting Information Figure S1B (normalized to local temperature maximum). For CP, the highest temperature increase was 20.5 mK (in the lower left corner of the map). At the same location, OP and NM generated 1.9 mK and 0.9 mK, respectively, with the same forward power.

The ratios between the different transmission modes are displayed in Figure 7A. OP and NM reduced the induced voltages by a factor ≥2 in 99% and 93%, respectively, of the mapped area, compared to CP. The statistical results are shown in Figure 7B. The induced voltages for the CP have a median of 27.7 mV, whereas the OP and NM have 0.63 mV and 0.56 mV median values, respectively. The SDs for the OP and NM are 1.57 mV and 3.76 mV.

4.1.4 | $\boldsymbol{Q}_S^T$ based pTx mitigation

Raw data to derive $\boldsymbol{Q}_S^T$ and subsequent mitigation results are presented in Figure 8. These lengthier acquisitions were only performed at seven positions (Figure 8A). Only three locations are shown and the complete figure is found in the Supporting Information Figure S4. The $\boldsymbol{Q}_S^T$ matrices (Figure 8B) are displayed together with diode (Figure 8C) and thermistor (Figure 8D) signals for the excitation modes WC, CP, OP, and NM. For comparison, the results for $\boldsymbol{Q}_S^E$ and the sensor signals for $\boldsymbol{Q}_S^E$ derived mitigation modes at these locations are depicted in (Figure 8E-G). It can be seen that diode and thermistor signals correlate well and describe the momentary patient hazard consistently.

$\boldsymbol{Q}_S^T$ based pTx mitigation was successful at all locations, with both OP and NM showing reduced heating compared to CP mode. Notably, the $\boldsymbol{Q}_S^T$ based OP mode outperformed both the $\boldsymbol{Q}_S^E$ based OP mode and the $\boldsymbol{Q}_S^T$ based NM mitigation. For NM, the picture is reversed in so far as the $\boldsymbol{Q}_S^E$ based variant performed better than the $\boldsymbol{Q}_S^T$ version in most but not all locations. These are minor differences, however; generally, all four mitigation modes perform well.

The dominant channel combinations show similar patterns for $\boldsymbol{Q}_S^E$ and $\boldsymbol{Q}_S^T$; only the number of non-zero entries are higher in $\boldsymbol{Q}_S^T$. As expected, the coupled amplitudes are highest in locations toward the edge of the phantom.

4.2 | MR experiments

4.2.1 | Prediction of RF-induced heating using a two-channel body coil

Figure 9A depicts temperature curves during a GRE sequence under varying flip angles. Measurement precision and noise level under pulsed gradient and RF conditions are not noticeably different from the testbed case (cf. Figure 5C). The transmitted RF power correlates well with the temperature increase (Figure 9B). In two-channel pTx experiments using the dual-drive body coil, $\boldsymbol{Q}_S^T$ becomes a 2×2 matrix and the temperature curves for its four elements are shown in Figure 9C. Once $\boldsymbol{Q}_S^T$ is known, the heating rate for arbitrary excitations can be predicted (Figure 9D). This procedure was repeated at another location, first $\mathbf{Q}_S^T$ was measured (Figure 9E) and then used to predict RF-induced implant heating for different transmit modes. The measured temperature increases after 5 s (Figure 9F) were 2.9 mK and 1.0 mK, while 2.4 mK and 0.8 mK were predicted.

4.2.2 | Eight-channel pTx mitigation and imaging

MRI results for $\boldsymbol{Q}_S^E$ based mitigation using the eight-channel pTx system and head coil are shown in Figure 10. Panels A to D show coronal and panels E to H axial images at the location of the red cursor for the transmission modes WC, B_1-shim, OP, and NM. The "B_1-shim" based on previously acquired relative B_1^+-maps is defined as equal amplitudes per channel and phases set for maximum B_1^+ at the position of the red cursor. The B_0 artifact due to the RMS sensors can be seen at the tip of the implant in the coronal images.

Image signal-to-noise ratios (SNRs) (Figure 10I-K) were extracted for all transmission modes along the dotted lines indicated in the images. It can be seen that OP mode was derived from the B_1-shim as their profiles coincide almost everywhere, only the imaging artifact near the implant is much reduced for OP. NM also reduces this artifact but at the cost of an overall degraded image quality. The diode signals at the implant tip are shown in Figure 10L. As expected, WC shows the highest values (142.2 mV), followed by B_1-shim (15.6 mV) and the mitigation modes NM (5.9 mV) and OP (0.9 mV).

5 | DISCUSSION

The presented results demonstrate that small and low-cost RMS sensors, ie, a diode and a thermistor, can be used to substantially reduce the risk for RF-induced heating in an

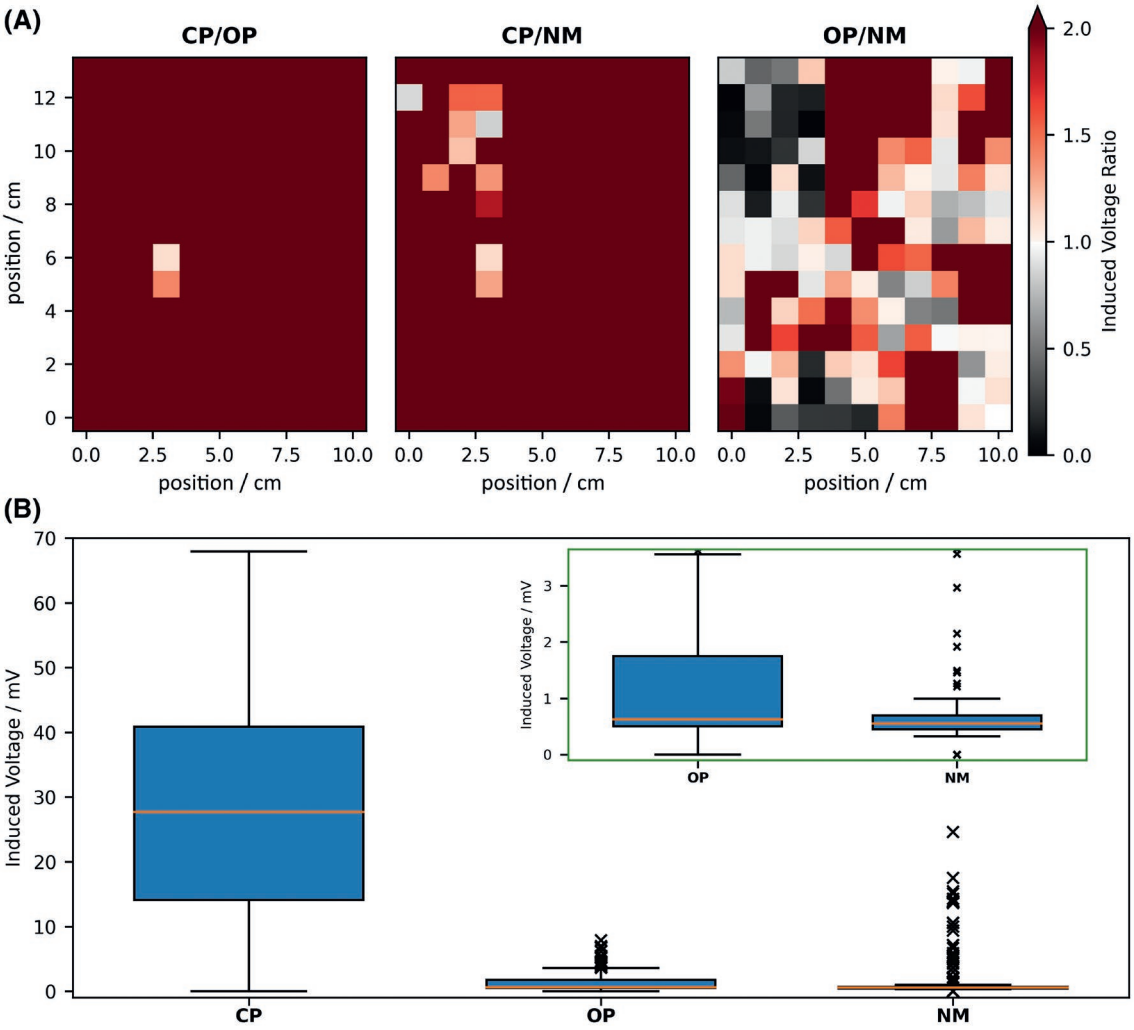

FIGURE 7 A, The induced voltage ratios are shown for each acquired mode. Both OP and NM reduces power at nearly all positions (99%). More than 2 times reduction is obtained in 95% of the positions. B, Box plot of induced voltages for CP, OP and NM excitation using Tukey's original definition.[94] The orange line indicates the median (50 percentile), the box 25 (Q1) and 75 (Q3) percentile (interquartile range, IQR), the whiskers are minimum datum above Q1-1.5*IQR and maximum datum below Q3+1.5*IQR and the crosses outliers. The smaller plot shows the zoomed OP and NM values as their median is close to zero

implant. The $\boldsymbol{Q_S}$ approach allows pTx-based mitigation of implant related RF hazards based solely on this sensor signal. This novel safety approach was successfully tested in testbed measurements at 7T frequency and with a pTx capable 3T MRI.

5.1 | Hazard mitigation

Both $\boldsymbol{Q_S^T}$ and $\boldsymbol{Q_S^E}$ based pTx mitigations were able to reduce RF-induced *E*-fields and temperatures at the implant tip compared to reference modes (CP or B_1-shim).

In testbed experiments at 300 MHz, the *E*-field signal could be reduced everywhere and by a factor ≥2 in 98% of the investigated area. In both testbed and MR experiments, the thermistor allowed tip temperature measurements with high temporal (~25 Hz) and temperature precision (~100 μK) which is not currently possible with fiberoptic probes.[29] This sensitivity enables safe and fast $\boldsymbol{Q_S^T}$ acquisitions with low RF power and the accurate assessment of higher temperature changes for the purpose of safety monitoring (Supporting Information Figure S2).

In principle, a single $\boldsymbol{Q_S}$ acquisition per subject and position is sufficient to ensure safe scanning as described before. Repeated acquisitions before each new sequence might be safer, however, in case of patient motion, changes of electromagnetic or thermal properties such as perfusion, and they are mandatory for 'moving implants', ie, during interventional procedures. In particular, the diode sensor is real time capable, as $\boldsymbol{Q_S^E}$ acquisition and calculation of an implant-friendly transmission vector take only ~ 20ms. $\boldsymbol{Q_S^T}$ acquisition, on the other hand, takes around ~ 1min for an eight-channel coil and ~ 4s for a two-channel body coil. These fast and precise temperature measurements allow accurate correlation between

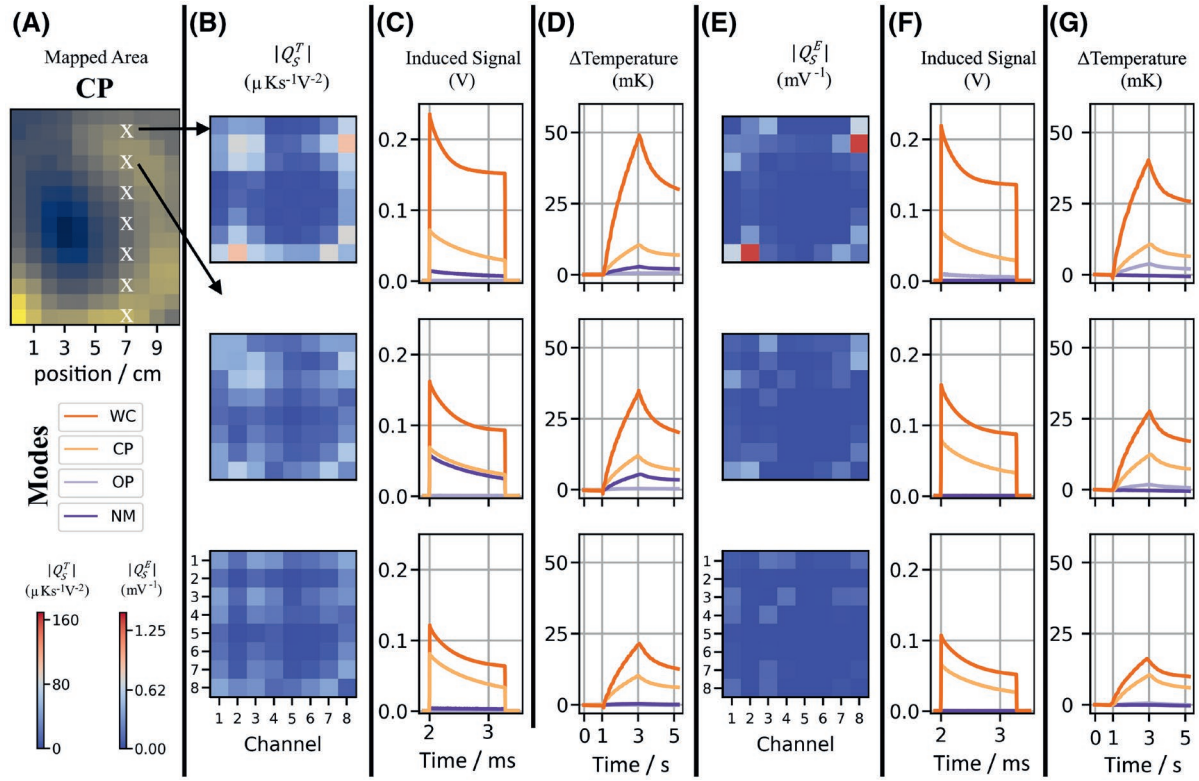

FIGURE 8 Testbed results at 300 MHz. A, The results of the $\boldsymbol{Q}_S$ experiment is shown in the selected locations indicated by the white crosses. B, The channel amplitudes of the resulted $\boldsymbol{Q}_S^T$ are shown. The induced currents resulted from the pTx mitigations based on the $\boldsymbol{Q}_S^T$ (C) and 2 s long temperature experiments using the $\boldsymbol{Q}_S^T$ (D). (E) Amplitudes of the $\boldsymbol{Q}_S^E$ at the same location of the $\boldsymbol{Q}_S^T$ and the same transmit power. The induced currents resulted from the pTx mitigations of $\boldsymbol{Q}_S^E$ (F) and 2 s long temperature experiments based on the $\boldsymbol{Q}_S^E$ (G). The complete figure including all measured locations is found as Supplementary Information Figure S4

dT/dt and SAR; therefore, much slower effects (eg, perfusion) can be ignored for pTx mitigation.

The body coil experiments demonstrate how temperature increase can be predicted for any phase and amplitude setting using $\boldsymbol{Q}_S^T$. However, a small over-/underestimation is visible (Figure 9D,F). This estimation error might be explained by the low RF power applied (the measurements are close to the sensitivity limit of the thermistors) and drifting background temperature of the phantom, which was not compensated.

While the diode gives *E*-field information, the thermistor provides temperature. Both quantities have their advantages and disadvantages. A field-based mitigation approach is faster and can be directly related to SAR, which is at present the most widely used metric in the RF safety context.[3,4] A diode signal can therefore easily be integrated into existing pTx safety approaches, eg, based on electromagnetic field simulations and virtual observation points.[65] As long as the implant affects the RF field distribution mostly locally, the sensor information can be combined with precomputed voxel models of the native human (without implants) to assess local SAR for arbitrary pTx pulses everywhere in the body. $\boldsymbol{Q}_S^T$, on the other hand, is a more direct safety measure as tissue is damaged by temperature, not SAR.[66-69] Thermal processes like perfusion or thermal conductivity of tissue and implant affect the temperature evolution,[46,70,71] and the thermal burden to the tissue may be moderate despite high *E*-fields. Overly conservative power limits could be avoided in such cases by an implant safety assessment rooted in temperature. In general, a combination of both field and temperature information, would allow field-based pTx mitigation in real time together with temperature monitoring in situ to evaluate and update the applied thermal dose. Two independent sensor signals have the additional advantage to make this approach more robust and failsafe.

5.2 | Advantages and limitations

It is important to highlight that the $\boldsymbol{Q}_S$ approach measures and mitigates field and temperatures directly at the hotspot location of the implant. All subject-specific parameters such as implant trajectory and location or the electrical parameters of the surrounding tissues are already included. This is a big advantage compared to simulation-based assessments, where a few voxel models are investigated instead of the real patient which leaves substantial room for error. eg, only a small variation of the implant location by 5 mm, may change the induced fields by a factor of 5.[29]

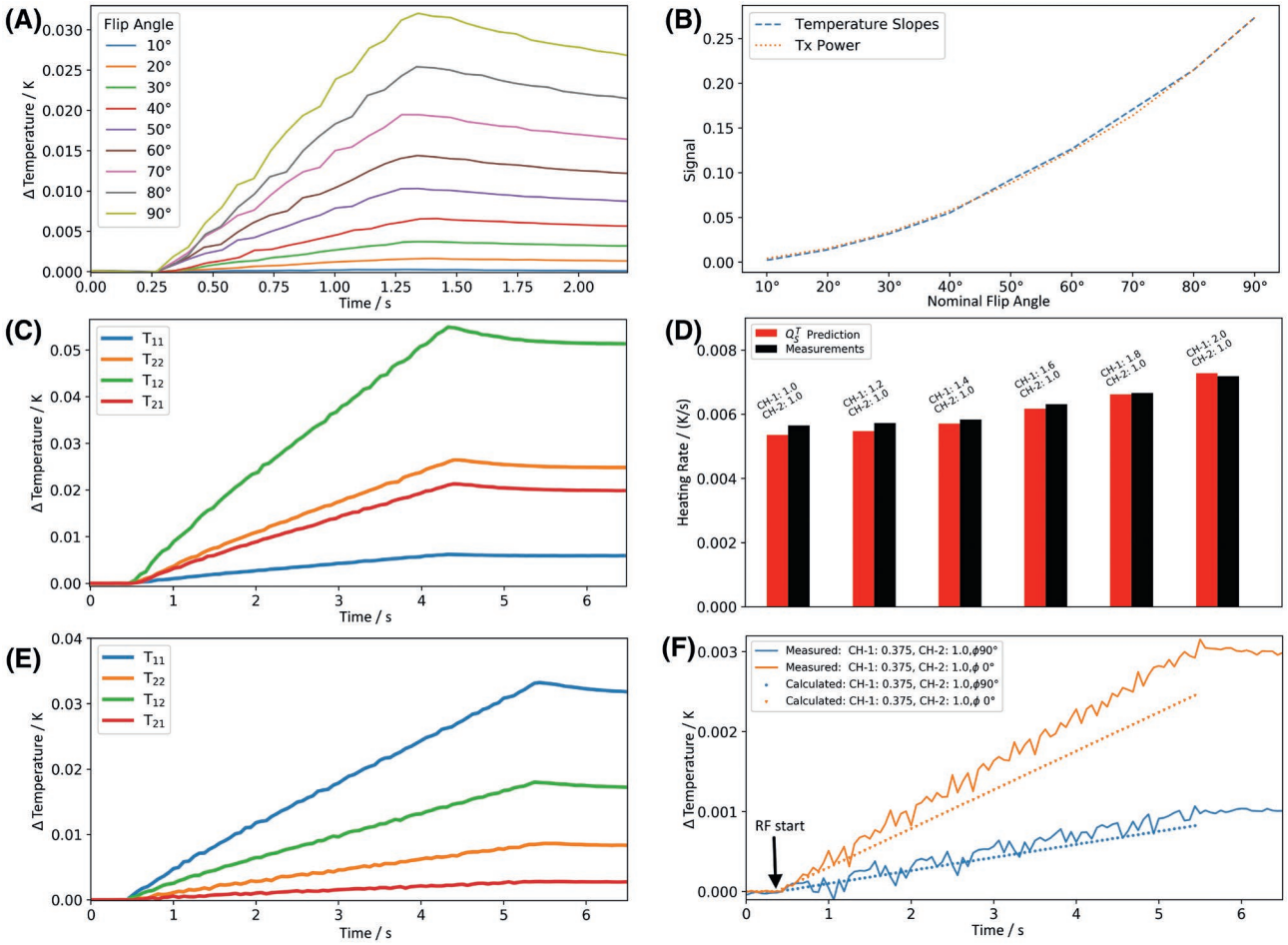

FIGURE 9 Prediction of RF-induced heating based on $\boldsymbol{Q}_S^T$ thermistor measurements inside a pTx capable 3T MRI. A two-channel birdcage body coil was used for transmission. A, Temperature rise deduced from the thermistor vs. nominal flip angle. B, Temperature slope vs measured transmitted power. C, $\boldsymbol{Q}_S^T$ raw data (4 measurements in total; based on the two-channel system). D, Temperature slopes measured during MRI for different excitation voltages vs $\boldsymbol{Q}_S^T$ based prediction of temperature slopes. $\boldsymbol{Q}_S^T$ raw data from a second location (E) and the corresponding temperature increase for different complex excitation vectors compared to $\boldsymbol{Q}_S^T$ based predictions of the temperature increase (F). $\boldsymbol{Q}_S^T$ acquisition can be performed with implant tip heating <0.1 K

A limitation of the presented work is that no calibration was performed to assess absolute induced signals and relate them to tissue temperatures. Even though pTx mitigation should be robust to changes in electromagnetic and thermal tissue properties, a tissue dependent calibration using standardized phantoms and fields[37,72,73] is needed for absolute thermal dose assessment.[66,68] Independent of this calibration, assessment of the thermal dose might be challenging in particular for applications where background field and electromagnetic tissue parameters change simultaneously eg, for interventional MR. It needs to be investigated further if multiple $\boldsymbol{Q}_S$ acquisitions or additional simulation-based evaluations of the underlying uncertainties might improve the results. Another important limitation is its exclusive focus on the implant: unlike simulations, the sensor tells nothing about the rest of the body. $\boldsymbol{Q}_S$ can only be one part of a comprehensive safety concept, therefore.

The implant cable carrying the measured diode signals acts as a transmission line.[74,75] This transmission line may contribute to erroneous E-field measurements.[76] Here, $\boldsymbol{Q}_S^E$ elements were extracted from 200 μs long RF pulses (ie, modulation frequency, $f_m = 5$ kHz) in all pTx experiments. The corresponding dT/dt measurements were significantly in agreement with the measured induced voltages (Figure 6) validating the E-field probe measurements.[77] Further increases in f_m may generate errors; however, once the circuit model is known, the corresponding sensor signal can be determined.[76,77]

All results were achieved with simple mock implants. The use of simplified models or mock implants is, however, common practice in the literature on implant safety in MRI.[25,28,32,33,37,78-83] It is undoubtedly possible to equip real-life implants with sensors, eg, with interventional devices this is a well-known common practice.[50,84,85] The sensor approach is designed for wire-like implants and requires a

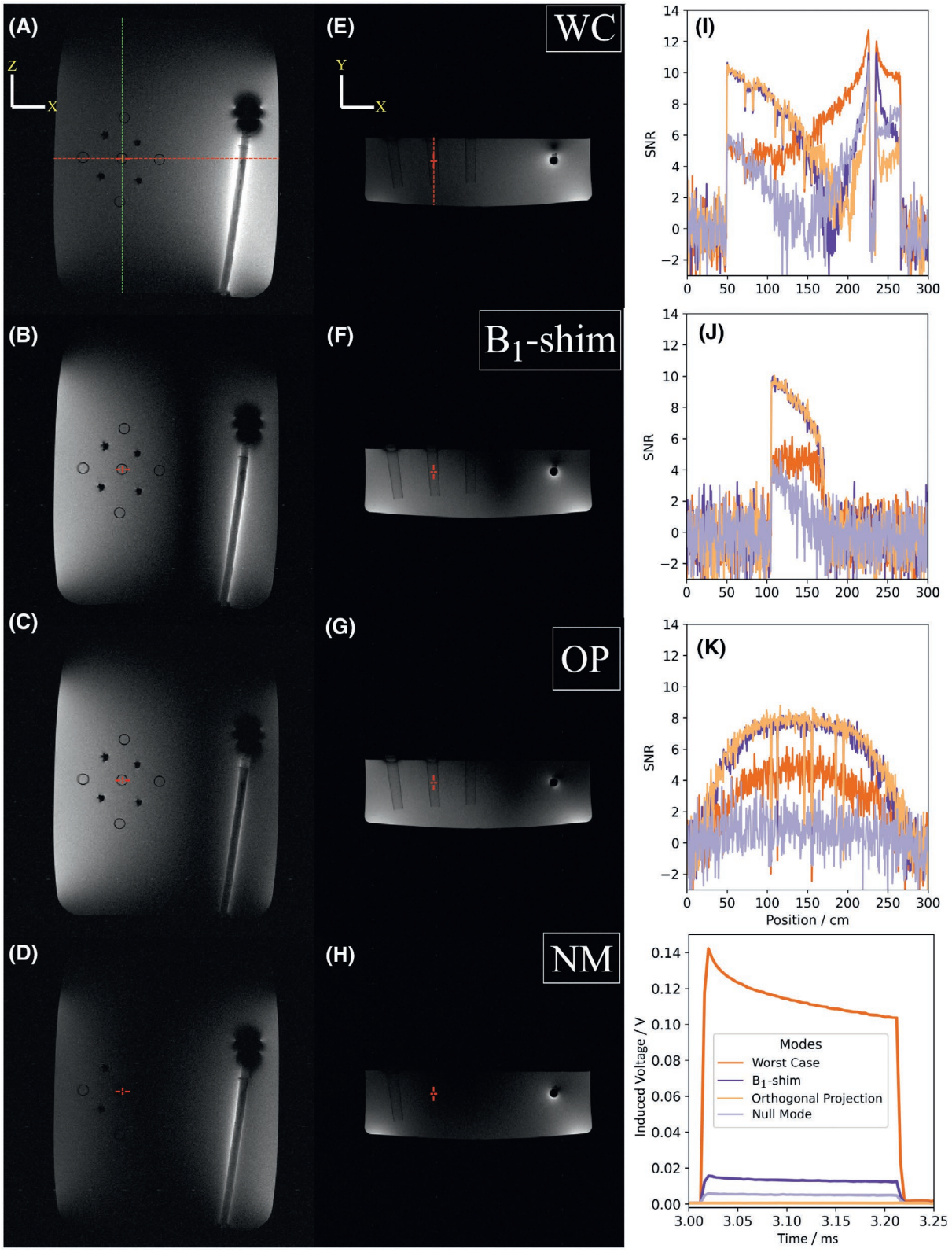

FIGURE 10 MRI experiments using eight-channel pTx. Q_S^E is obtained using the diode signal (eight-channels, 64 measurements). Red cross from the 3T MRI images marks the selected shim location for the imaging. The coronal (A-D) and axial (E-H) images of the four different modes: WC, B_1-shim, OP, and NM, respectively. SNR for all pTx excitations along x-axis (I; red-dotted line in A), y-axis (J; red-dotted line in E), and z-axis (K; green dotted line in A). B_1-shim and OP have very similar image profiles. L, Induced diode signals on the implant for all pTx modes. OP and NM show substantially smaller induced voltages compared to WC and B_1-shim

priori knowledge of the hot spot location. Usually, this is the tip end since, among other reasons, everywhere else the implant is insulated and heating via capacitive coupling alone is uncritical. For hypothetical implants with more than one hot spot, the extension of $\boldsymbol{Q_S}$ to multiple sensors would be straightforward.

Previous works used current sensors,[28,49,86] or time-domain *E*-field probes,[29,87] which detect phase sensitive information. The advantage of the presented RMS sensors is their small footprint (<1.5 mm^3), low-cost, and simple readout electronics. Geometrically, it should always be feasible to position these sensors directly where the maximum heating is expected. Thus, ensuring maximum sensitivity, while avoiding measurements at current null positions, which do not necessarily correspond to a tip current null, eg, due to wavelength effects. Even though designs exist to eg, integrate diodes in electrodes,[88] positioning of RMS sensors at the implant tip may not be feasible without impairing the functionality of the medical implant. However, sensor location is not necessarily restricted to the implant tip. As an example, we performed experiments with a third mock implant where the diode position is 4 cm away from the implant tip (Supporting Information Figure S3). This configuration does not alter the implant tip geometry, is completely embedded within the implant and can accurately correlate flip angle to induced sensor values even for low transmit powers. The thermistor on the other hand needs to be close to the temperature hotspot using high thermal conductive components for coating in order to reflect tissue temperature more accurately. eg, it has been demonstrated that a thermistor was successfully used with a silver electrode in MRI heating experiments.[46]

Even though it was not the objective of this work to visualize the implant tip,[2,49,89,90] a disadvantage shown in our data are the strong susceptibility artifacts of the embedded sensors that are visible around the implant tip (Figure 10A-D). A possible explanation might be nickel oxide in the NTCs and/or the used solder metal. Other works show less severe susceptibility artifacts using off-the-shelf NTCs[46] and it is reasonable to assume that MR compatible RMS sensors will become available similar to the availability of non-magnetic ceramic capacitors used eg, in RF coils. Another solution is to place the diode for $\boldsymbol{Q_S^E}$ based pTx mitigation a few cm away from the tip, which shifts the susceptibility artefact away from the implant tip (Supporting Information Figure S3). With such a configuration, $\boldsymbol{Q_S}$ could then also be applied to visualize the complete guidewire eg, by a difference image between a (low-flip angle) CP or WC excitation (strong B_1^+ magnitude the implant, Figure 10A-B) and the OP (weaker B_1^+ magnitude around the implant, Figure 10C) imaging-mode.[49]

Compared to imaging-based pTx mitigation techniques,[43,44,46,48] no B_1^+-mapping or other pre-scans need to be applied, which might be susceptible to errors and are still not real time capable, although they have tremendously improved over decades.[42,45,47,48]

In our present implementation a lead is used to sample the diode and thermistor signals. In real implants, system-on-chip or wireless solutions,[46,91,92] would enable a more convenient communication between MR scanner and implant. Wireless communication for implants is already regulated and many AIMDs are appearing on the market applying such technology. The necessity to get the signal from the tip to the communications chip, typically in the generator housing, would persist, however. This could be achieved by a thin extra lead but more intelligent solutions are conceivable.[93]

5.3 | OP and NM

To illustrate the versatility of the $\boldsymbol{Q_S}$ approach, two different mitigation modes were applied in this work, null modes and orthogonal projection. While these are application examples and not the main subject of the paper, a brief comparison may still be worthwhile. Both showed similar performance in terms of reduction factors compared to the CP mode, while $\boldsymbol{Q_S^E}$ based NM reduction was slightly higher, compared to OP, in 62% of the investigated 154 locations. OP was able to reduce the tip voltage everywhere, compared to CP, while for NM it was 14% and 17% higher than CP at two locations. This might be attributed to the fact, that only a single null mode was used for pTx mitigation and a different eigenvector or combination of multiple null modes would further improve these results.[28] In terms of mitigation, both modes work well, in general.

The main advantage of the OP method is the underlying imaging information that is partially preserved in the transmission vector. As such, any B_1^+-shim setting or standard CP can be used as a basis for pTx mitigation in the OP mode without the need for any additional acquisition or simulation.[29] Using only a single NM degrades imaging quality substantially (Figure 10); however, in principle a linear combination of different NMs can be used for B_1^+-shimming, if B_1^+-profiles for these NMs are acquired beforehand.[28]

6 | CONCLUSIONS

A novel safety strategy for pTx-based MR systems is presented; based on RMS sensors embedded in an implant and the $\boldsymbol{Q_S}$ formalism. In this explorative study, RF-induced heating could be successfully mitigated in mock implants, while maintaining B_1^+. The proposed approach is real-time capable, patient and exam specific and solely based on the embedded sensor signals. No additional electromagnetic field simulations or a priori safety testing in vitro is required. The presented results suggest that "smart" implants with embedded

sensors, communicating with a scanner, may well be a promising concept toward safe scanning of patients with implants.

ACKNOWLEDGMENTS

This project (17IND01 MIMAS) has received funding from the EMPIR programme co-financed by the Participating States and from the European Union's Horizon 2020 research and innovation program. Open Access funding enabled and organized by Projekt DEAL

ORCID

Berk Silemek https://orcid.org/0000-0001-8227-3632
Johannes Petzold https://orcid.org/0000-0001-9503-0998
Bernd Ittermann https://orcid.org/0000-0002-4087-471X
Lukas Winter https://orcid.org/0000-0002-4381-275X

REFERENCES

1. Winter L, Seifert F, Zilberti L, Murbach M, Ittermann B. MRI-related heating of implants and devices: a review. *J Magn Reson Imaging*. 2021;53:1646-1665.
2. Barkhausen J, Kahn T, Krombach G, et al. White paper: interventional MRI: current status and potential for development considering economic perspectives, Part 1: general application. *RöFo - Fortschritte Auf Dem Geb Röntgenstrahlen Bildgeb Verfahr*. 2017;189:611-623.
3. *ISO-TS 10974:2018(E) Assessment of the Safety of Magnetic Resonance Imaging for Patients with an Active Implantable Medical Device*. Geneva, Switzerland: International Organization for Standardization; 2018. https://www.iso.org/standard/65055.html
4. *ASTM F2182-11a Standard Test Method for Measurement of Radio Frequency Induced Heating near Passive Implants during Magnetic Resonance Imaging*. West Conshohocken, PA: ASTM International; 2011. https://doi.org/10.1520/F2182-11A
5. Neufeld E, Kühn S, Szekely G, Kuster N. Measurement, simulation and uncertainty assessment of implant heating during MRI. *Phys Med Biol*. 2009;54:4151-4169.
6. Russo R. Determining the risks of clinically indicated nonthoracic magnetic resonance imaging at 1.5 T for patients with pacemakers and implantable cardioverter-defibrillators: rationale and design of the MagnaSafe Registry. *Am Heart J*. 2013;165:266-272.
7. Russo RJ, Costa HS, Silva PD, et al. Assessing the risks associated with MRI in patients with a pacemaker or defibrillator. *N Engl J Med*. 2017;376:755-764.
8. Rahsepar AA, Zimmerman SL, Hansford R, et al. The relationship between MRI radiofrequency energy and function of non-conditional implanted cardiac devices: a prospective evaluation. *Radiology*. Published online March 3, 2020;295:307-313.
9. Gupta SK, Ya'qoub L, Wimmer AP, Fisher S, Saeed IM. Safety and clinical impact of MRI in patients with non–MRI-conditional cardiac devices. *Radiol Cardiothorac Imaging*. 2020;2:e200086.
10. Vigen KK, Reeder SB, Hood MN, et al. Recommendations for imaging patients with cardiac implantable electronic devices (CIEDs). *J Magn Reson Imaging*. 2021;53:1311-1317.
11. Jech R, Urgošík D, Tintěra J, et al. Functional magnetic resonance imaging during deep brain stimulation: a pilot study in four patients with Parkinson's disease. *Mov Disord*. 2001;16:1126-1132.
12. Larson PS, Richardson RM, Starr PA, Martin AJ. Magnetic resonance imaging of implanted deep brain stimulators: experience in a large series. *Stereotact Funct Neurosurg*. 2008;86:92-100.
13. Nazzaro JM, Lyons KE, Wetzel LH, Pahwa R. Use of brain MRI after deep brain stimulation hardware implantation. *Int J Neurosci*. 2010;120:176-183.
14. Weise LM, Schneider GH, Kupsch A, Haumesser J, Hoffmann KT. Postoperative MRI examinations in patients treated by deep brain stimulation using a non-standard protocol. *Acta Neurochir (Wien)*. 2010;152:2021-2027.
15. Knight EJ, Testini P, Min H-K, et al. Motor and nonmotor circuitry activation induced by subthalamic nucleus deep brain stimulation in patients with Parkinson disease: intraoperative functional magnetic resonance imaging for deep brain stimulation. *Mayo Clin Proc*. 2015;90:773-785.
16. Arantes PR, Cardoso EF, Barreiros MÂ, et al. Performing functional magnetic resonance imaging in patients with Parkinson's disease treated with deep brain stimulation. *Mov Disord*. 2006;21:1154-1162.
17. Sammartino F, Krishna V, Sankar T, et al. 3-Tesla MRI in patients with fully implanted deep brain stimulation devices: a preliminary study in 10 patients. *J Neurosurg*. 2016;127:892-898.
18. Fiveland E, Madhavan R, Prusik J, et al. EKG-based detection of deep brain stimulation in fMRI studies. *Magn Reson Med*. 2018;79:2432-2439.
19. Davidson B, Tam F, Yang B, et al. Three-tesla magnetic resonance imaging of patients with deep brain stimulators: results from a phantom study and a pilot study in patients. *Neurosurgery*. 2021;88:349-355.
20. DiMarzio M, Madhavan R, Hancu I, et al. Use of functional MRI to assess effects of deep brain stimulation frequency changes on brain activation in Parkinson disease. *Neurosurgery*. 2021;88:356-365.
21. Seifert F, Rinneberg H. Adaptive coil control: SNR optimization of a TR volume coil for single voxel MRS at 3T. In: Intl. Soc. Mag. Reson. Med. Vol 10. 2002, p. 162.
22. Zhu Y. Parallel excitation with an array of transmit coils. *Magn Reson Med*. 2004;51:775-784.
23. Ullmann P, Junge S, Wick M, Seifert F, Ruhm W, Hennig J. Experimental analysis of parallel excitation using dedicated coil setups and simultaneous RF transmission on multiple channels. *Magn Reson Med*. 2005;54:994-1001.
24. Katscher U, Börnert P, Leussler C, van den Brink JS. Transmit SENSE. *Magn Reson Med*. 2003;49:144-150.
25. Eryaman Y, Akin B, Atalar E. Reduction of implant RF heating through modification of transmit coil electric field. *Magn Reson Med*. 2011;65:1305-1313.
26. Seifert F, Weidemann G, Ittermann B. Q matrix approach to control implant heating by transmit array coils. In: 23rd Annual Meeting of ISMRM. 2015, p. 3212.
27. Eryaman Y, Guerin B, Akgun C, et al. Parallel transmit pulse design for patients with deep brain stimulation implants. *Magn Reson Med*. 2015;73:1896-1903.
28. Etezadi-Amoli M, Stang P, Kerr A, Pauly J, Scott G. Controlling radiofrequency-induced currents in guidewires using parallel transmit. *Magn Reson Med*. 2015;74:1790-1802.
29. Winter L, Silemek B, Petzold J, et al. Parallel transmission medical implant safety testbed: real-time mitigation of RF induced tip heating using time-domain E-field sensors. *Magn Reson Med*. 2020;84:3468-3484.

30. Petzold J, Ittermann B, Seifert F. Robustness of pTx safety concepts to varying subjects and subject positions. *Int Soc Magn Reson Med*. 2021:#2488.
31. Guerin B, Angelone LM, Dougherty D, Wald LL. Parallel transmission to reduce absorbed power around deep brain stimulation devices in MRI: impact of number and arrangement of transmit channels. *Magn Reson Med*. 2020;83:299-311.
32. Córcoles J, Zastrow E, Kuster N. Convex optimization of MRI exposure for mitigation of RF-heating from active medical implants. *Phys Med Biol*. 2015;60:7293-7308.
33. McElcheran CE, Yang B, Anderson KJT, Golenstani-Rad L, Graham SJ. Investigation of parallel radiofrequency transmission for the reduction of heating in long conductive leads in 3 Tesla magnetic resonance imaging. *PLoS One*. 2015;10:e0134379.
34. McElcheran CE, Yang B, Anderson KJT, Golestanirad L, Graham SJ. Parallel radiofrequency transmission at 3 tesla to improve safety in bilateral implanted wires in a heterogeneous model. *Magn Reson Med*. 2017;78:2406-2415.
35. Yang B, Wei PS, McElcheran CE, Tam F, Graham SJ. A platform for 4-channel parallel transmission MRI at 3 T: demonstration of reduced radiofrequency heating in a test object containing an implanted wire. *J Med Biol Eng*. 2019;39:835-844.
36. McElcheran CE, Golestanirad L, Iacono MI, et al. Numerical simulations of realistic lead trajectories and an experimental verification support the efficacy of parallel radiofrequency transmission to reduce heating of deep brain stimulation implants during MRI. *Sci Rep*. 2019;9:1-14.
37. Guerin B, Iacono MI, Davids M, Dougherty D, Angelone LM, Wald LL. The "virtual DBS population": five realistic computational models of deep brain stimulation patients for electromagnetic MR safety studies. *Phys Med Biol*. 2019;64:035021.
38. Mattei E, Triventi M, Calcagnini G, et al. Complexity of MRI induced heating on metallic leads: experimental measurements of 374 configurations. *Biomed Eng Online*. 2008;7:11.
39. Rezai AR, Finelli D, Nyenhuis JA, et al. Neurostimulation systems for deep brain stimulation: in vitro evaluation of magnetic resonance imaging-related heating at 1.5 Tesla. *J Magn Reson Imaging*. 2002;15:241-250.
40. Nordbeck P, Weiss I, Ehses P, et al. Measuring RF-induced currents inside implants: impact of device configuration on MRI safety of cardiac pacemaker leads. *Magn Reson Med*. 2009;61:570-578.
41. Venook RD, Overall WR, Shultz K, Conolly S, Pauly JM, Scott GC. Monitoring induced currents on long conductive structures during MRI. In: *Proceedings: ISMRM 16th Scientific Meeting & Exhibition*, 2008, Toronto, Ontario, Canada. p. 898.
42. van den Bosch MR, Moerland MA, Lagendijk JJW, Bartels LW, van den Berg CAT. New method to monitor RF safety in MRI-guided interventions based on RF induced image artefacts. *Med Phys*. 2010;37:814-821.
43. Overall WR, Pauly JM, Stang PP, Scott GC. Ensuring safety of implanted devices under MRI using reversed RF polarization. *Magn Reson Med*. 2010;64:823-833.
44. Eryaman Y, Turk EA, Oto C, Algin O, Atalar E. Reduction of the radiofrequency heating of metallic devices using a dual-drive birdcage coil. *Magn Reson Med*. 2013;69:845-852.
45. Griffin GH, Anderson KJT, Celik H, Wright GA. Safely assessing radiofrequency heating potential of conductive devices using image-based current measurements. *Magn Reson Med*. 2015;73:427-441.
46. Silemek B, Acikel V, Oto C, et al. A temperature sensor implant for active implantable medical devices for in vivo subacute heating tests under MRI. *Magn Reson Med*. 2018;79:2824-2832.
47. Griffin GH, Ramanan V, Barry J, Wright GA. Toward in vivo quantification of induced RF currents on long thin conductors. *Magn Reson Med*. 2018;80:1922-1934.
48. Eryaman Y, Kobayashi N, Moen S, et al. A simple geometric analysis method for measuring and mitigating RF induced currents on deep brain stimulation leads by multichannel transmission/reception. *Neuroimage*. 2019;184:658-668.
49. Godinez F, Scott G, Padormo F, Hajnal JV, Malik SJ. Safe guidewire visualization using the modes of a PTx transmit array MR system. *Magn Reson Med*. 2020;83:2343-2355.
50. Iwasawa J, Koruth JS, Petru J, et al. Temperature-controlled radiofrequency ablation for pulmonary vein isolation in patients with atrial fibrillation. *J Am Coll Cardiol*. 2017;70:542-553.
51. Kautzner J, Albenque J-P, Natale A, et al. A novel temperature-controlled radiofrequency catheter ablation system used to treat patients with paroxysmal atrial fibrillation. *JACC Clin Electrophysiol*. 2021;7:352-363.
52. Silemek B, Winter L, Seifert F, et al. Real-time safety assessment and mitigation of RF induced implant heating with parallel transmission and low-cost RMS sensors. In: *Proceedings of the ISMRM & SMRT Virtual Conference & Exhibition*. 2020, p. 4196.
53. Silemek B, Seifert F, Ittermann B, Winter L. Safe scanning of elongated implants with the sensor matrix Qs: comparison of orthogonal projection and null mode based pTx mitigation. In: *29th Annual Meeting of ISMRM*. 2021, p. 362.
54. Silemek B, Winter L, Seifert F, Pfeiffer H, Ittermann B. Measurement-based safety assessment, prediction and mitigation of RF induced implant heating with parallel transmission: temperature matrix. In: *28th Annual Meeting of ISMRM*. 2020, p. 1135.
55. Graesslin I, Homann H, Biederer S, et al. A specific absorption rate prediction concept for parallel transmission MR. *Magn Reson Med*. 2012;68:1664-1674.
56. Bardati F, Borrani A, Gerardino A, Lovisolo GA. SAR optimization in a phased array radiofrequency hyperthermia system. *IEEE Trans Biomed Eng*. 1995;42:1201-1207.
57. Silemek B, Açıkel V, Atalar E. RF safety of active implantable medical devices. *eMagRes.* 2019;8:103-120.
58. Yeung CJ, Atalar E. A Green's function approach to local RF heating in interventional MRI. *Med Phys*. 2001;28:826-832.
59. Boulant N, Wu X, Adriany G, Schmitter S, Uğurbil K, Van de Moortele P-F. Direct control of the temperature rise in parallel transmission by means of temperature virtual observation points: Simulations at 10.5 tesla. *Magn Reson Med*. 2016;75:249-256.
60. Bassen H, Smith G. Electric field probes–A review. *IEEE Trans Antennas Propag*. 1983;31:710-718.
61. Stuchly MA, Kraszewski A, Stuchly SS. Implantable electric-field probes—some performance characteristics. *IEEE Trans Biomed Eng*. 1984;BME-31:526-531.
62. Kaatee RSJP, van Rhoon GC. An electric field measurement system, using a two-dimensional array of diodes. *Int J Hyperthermia*. 1999;15:441-454.
63. Seifert F, Pfeiffer H, Mekle R, Waxmann P, Ittermann B. 7T 8-channel PTx head coil with High B1+ efficiency optimized for MRS. In: 24th Annual Meeting of ISMRM. 2016, p. 3545.
64. Han H, Moritz R, Oberacker E, Waiczies H, Niendorf T, Winter L. Open source 3D multipurpose measurement system with

submillimetre fidelity and first application in magnetic resonance. *Sci Rep*. 2017;7:13452.
65. Eichfelder G, Gebhardt M. Local specific absorption rate control for parallel transmission by virtual observation points. *Magn Reson Med*. 2011;66:1468-1476.
66. Sapareto SA, Dewey WC. Thermal dose determination in cancer therapy. *Int J Radiat Oncol*. 1984;10:787-800.
67. Yarmolenko PS, Moon EJ, Landon C, et al. Thresholds for thermal damage to normal tissues: an update. *Int J Hyperthermia*. 2011;27:320-343.
68. Van Rhoon GC, Samaras T, Yarmolenko PS, Dewhirst MW, Neufeld E, Kuster N. CEM 43°C thermal dose thresholds: a potential guide for magnetic resonance radiofrequency exposure levels? *Eur Radiol*. 2013;23:2215-2227.
69. Murbach M, Neufeld E, Capstick M, et al. Thermal tissue damage model analyzed for different whole-body SAR and scan durations for standard MR body coils. *Magn Reson Med*. 2014;71:421-431.
70. Luechinger R, Zeijlemaker VA, Pedersen EM, et al. In vivo heating of pacemaker leads during magnetic resonance imaging. *Eur Heart J*. 2005;26:376-383.
71. Winter L, Oberacker E, Özerdem C, et al. On the RF heating of coronary stents at 7.0 Tesla MRI. *Magn Reson Med*. 2015;74:999-1010.
72. Klepsch T, Linde TD, Hoffmann W, Botterweck H, Ittermann B, Seifert F. Calibration of fibre-optic RF E/H-field probes using a magnetic resonance (MR) compatible TEM cell and dedicated MR measurement techniques. *Biomed Eng Biomed Tech*. 2012;57(SI-1-Track-B):119-122.
73. Christ A, Kainz W, Hahn EG, et al. The virtual family—development of surface-based anatomical models of two adults and two children for dosimetric simulations. *Phys Med Biol*. 2010;55:N23-N38.
74. Acikel V, Atalar E. Modeling of radio-frequency induced currents on lead wires during MR imaging using a modified transmission line method. *Med Phys*. 2011;38:6623-6632.
75. Özen AC, Lottner T, Bock M. Safety of active catheters in MRI: termination impedance versus RF-induced heating. *Magn Reson Med*. 2019;81:1412-1423.
76. Smith GS. Analysis of miniature electric field probes with resistive transmission lines. *IEEE Trans Microw Theory Tech*. 1981;29:1213-1224.
77. Meier K, Burkhardt M, Schmid T, Kuster N. Broadband calibration of E-field probes in lossy media. *IEEE Trans Microw Theory Tech*. 1996;44:1954-1962.
78. Park S-M, Kamondetdacha R, Nyenhuis JA. Calculation of MRI-induced heating of an implanted medical lead wire with an electric field transfer function. *J Magn Reson Imaging*. 2007;26:1278-1285.
79. Yeung CJ, Susil RC, Atalar E. RF safety of wires in interventional MRI: using a safety index. *Magn Reson Med*. 2002;47:187-193.
80. Tokaya JP, Raaijmakers AJE, Luijten PR, Bakker JF, van den Berg CAT. MRI-based transfer function determination for the assessment of implant safety. *Magn Reson Med*. 2017;78:2449-2459.
81. Tokaya JP, Raaijmakers AJE, Luijten PR, van den Berg CAT. MRI-based, wireless determination of the transfer function of a linear implant: introduction of the transfer matrix. *Magn Reson Med*. 2018;80:2771-2784.
82. Tokaya JP, van den Berg CAT, Luijten PR, Raaijmakers AJE. Explaining RF induced current patterns on implantable medical devices during MRI using the transfer matrix. *Med Phys*. 2021;48:132-141.
83. Yao A, Zastrow E, Neufeld E, Kuster N. Efficient and reliable assessment of the maximum local tissue temperature increase at the electrodes of medical implants under MRI exposure. *Bioelectromagnetics*. 2019;40:422-433.
84. Mukherjee RK, Chubb H, Roujol S, Razavi R, O'Neill MD. Advances in real-time MRI–guided electrophysiology. *Curr Cardiovasc Imaging Rep*. 2019;12:6.
85. Zuehlsdorff S, Umathum R, Volz S, et al. MR coil design for simultaneous tip tracking and curvature delineation of a catheter. *Magn Reson Med*. 2004;52:214-218.
86. Weidemann G, Seifert F, Ittermann B. Reduction of the E field at the tip of implanted wires generated by pTx coils using RF current measurements. In: *Proceedings: ISMRM 24th Annual Meeting & Exhibition 2016, Singapore*. p. 2216. http://archive.ismrm.org/2016/2216.html
87. Nordbeck P, Fidler F, Weiss I, et al. Spatial distribution of RF-induced E-fields and implant heating in MRI. *Magn Reson Med*. 2008;60:312-319.
88. Guerrero E, Polednik A, Ecker M, et al. Indium–gallium–zinc oxide Schottky diodes operating across the glass transition of stimuli-responsive polymers. *Adv Electron Mater*. 2020;6:1901210.
89. Hargreaves BA, Worters PW, Pauly KB, Pauly JM, Koch KM, Gold GE. Metal-induced artifacts in MRI. *Am J Roentgenol*. 2011;197:547-555.
90. Jungmann PM, Agten CA, Pfirrmann CW, Sutter R. Advances in MRI around metal. *J Magn Reson Imaging*. 2017;46:972-991.
91. Acikel V, Silemek B, Atalar E. Wireless control of induced radiofrequency currents in active implantable medical devices during MRI. *Magn Reson Med*. 2020;83(6):2370-2381.
92. Özen AC, Silemek B, Lottner T, Atalar E, Bock M. MR safety watchdog for active catheters: wireless impedance control with real-time feedback. *Magn Reson Med*. 2020;84:1048-1060.
93. Rav Acha M, Soifer E, Hasin T. Cardiac implantable electronic miniaturized and micro devices. *Micromachines*. 2020;11:902.
94. Tukey JW. *Exploratory Data Analysis* (Vol. 2). London: Addison-Wesley Publishing Company Reading; 1977:131-160.

SUPPORTING INFORMATION

Additional supporting information may be found online in the Supporting Information section.

FIGURE S1 Measured temperature profiles from the CP, OP and NM based excitations (Figure 6) based on the $\boldsymbol{Q}_S^E$ acquisition at 300 MHz in the testbed setup. (A) Absolute temperature differences and (B) normalized temperature differences to the local temperature maximum. A maximum temperature difference of 20.5 mK (x0y0) was found in CP mode for an applied RF pulse duration of 2 s. At this location the proposed pTx mitigation method reduced the temperature increase to 1.9 mK for OP and 0.9 mK for NM

FIGURE S2 A) RF-heating experiments with 2.87 W RF power applied over 300 s to implant#1 show a high-dynamic range of the thermistor-based temperature measurements. The temperature increase was 2.53 K. (B) Induced voltage measured at the diode for this particular RF heating transmission pulse of 1.2 ms length. For a temperature increase above 1°C, thermistor readings were previously compared to temperature measurements of fiber-optic temperature probes[29]

FIGURE S3 (A) Implant #3 with a diode placed 4 cm away from the implant tip, which was not altered. The diode was soldered to the inner conductor on anode and cathode and sealed using hot glue. (B) Coronal GRE 3T MR-image of the wire showing the shifted susceptibility artefact (signal void) of the diode below the implant tip. (C) Induced voltages measured at the diode for various applied flip angles (10°-90°). For a flip angle of 90°, the scanner reported time averaged RF power was 190 W with an excitation voltage of 393 V. For 10° flip angle, the applied time averaged RF power by the scanner is about 2 W. Each induced voltage resembles the envelope of the applied RF pulse. (D) Measured peak induced voltage versus applied flip angle. A good correlation (Pearson correlation is $r > 0.99$, $P < .001$) and high dynamic range of the diode signal can be seen. Even low flip angles can be distinguished correctly, without the need to position the diode at the implant tip and alter the implant tip electromagnetically

FIGURE S4 The complete Figure 8 including results of all seven locations of the testbed results at 300 MHz (A) The results of the $\boldsymbol{Q_S}$ experiment is shown in the selected locations indicated by the white crosses. (B) The channel amplitudes of the resulted $\boldsymbol{Q_S^T}$ are shown. (C) The induced currents resulted from the pTx mitigations based on the $\boldsymbol{Q_S^T}$ and (D) 2 s long temperature experiments using the $\boldsymbol{Q_S^T}$. (E) Amplitudes of the $\boldsymbol{Q_S^E}$at the same location of the $\boldsymbol{Q_S^T}$ and the same transmit power. (F) The induced currents resulted from the pTx mitigations of $\boldsymbol{Q_S^E}$ (G) 2 s long temperature experiments based on the $\boldsymbol{Q_S^E}$

How to cite this article: Silemek B, Seifert F, Petzold J, et al. Rapid safety assessment and mitigation of radiofrequency induced implant heating using small root mean square sensors and the sensor matrix Q_s. *Magn Reson Med*. 2022;87:509–527. https://doi.org/10.1002/mrm.28968